Journal of Alloys and Compounds 509 (2011) 2054–2059

Contents lists available at ScienceDirect

Journal of Alloys and Compounds

journal homepage: www.elsevier.com/locate/jallcom

Effect of bottom electrode and resistive layer on the dielectric and ferroelectric properties of sol–gel derived $BiFeO_3$ thin films

A. Huang, S.R. Shannigrahi*

*Institute of Materials Research and Engineering, A*STAR, Agency for Science, Technology and Research, Singapore 117602, Singapore*

ARTICLE INFO

Article history:
Received 14 July 2010
Received in revised form 22 October 2010
Accepted 22 October 2010
Available online 4 November 2010

Keywords:
Sol–gel
La_2O_3
RuO_2
$BiFeO_3$
Ferroelectric properties

ABSTRACT

The effect of RuO_2 electrodes and La_2O_3 resistive layer were analyzed on the electrical and ferroelectric properties of $BiFeO_3$ (BFO) films deposited on Pt/Ti/SiO_2/Si substrates using a chemical solution method. XRD patterns revealed that BFO films with RuO_2 and La_2O_3 layers appeared preferred (0 1 2) orientation. The surfaces of the BFO films with the La_2O_3 layer appeared uniform with dense grain clusters. The utilization of La_2O_3 and RuO_2 layers reduced the diffusion of Ti and Si into the BFO films. Leakage mechanism of the films found specific to applied electric field. At lower applied electric field space-charge-limited current found dominant and at an applied electric field >80 kV/cm surface-limited conduction (Fowler-Nordheim type) found the dominant. The BFO films grown with La_2O_3 resistive layers also contained lower concentrations of Fe^{2+}, which resulted enhancement of dielectric constant (ε), remnant polarization and lower leakage current. Among the studied films RuO_2/BFO/La_2O_3/BFO/RuO_2/Pt/Ti/SiO_2/Si exhibited the best with value of relative permittivity (ε_r) 208.8, leakage current 5.503×10^{-6} kV/cm^2, remnant polarization ($2P_r$) 3.80 μC/cm^2, and coercive field ($2E_c$) 78.22 kV/cm.

1. Introduction

In recent years multiferroic $BiFeO_3$ (BFO) is being studied extensively. BFO is antiferromagnetic with the Néel temperature ($T_N \approx 370\,^\circ$C) and ferroelectric with the Curie temperature ($T_C \approx 830\,^\circ$C) and probably be an excellent candidate for multiferroic applications [1–3]. However, the practical device realization of BFO has been hindered due to high leakage current, which mainly results from the presence of defects [4–6]. To reduce leakage current in BFO film, researchers considered ion substitutions in the Bi and/or Fe sites as well as by employing conducting oxide electrodes [7–12] and preparation of high-quality samples [13] to improve the electrical properties of BFO. The conducting oxide layers generally considered prevent inter-diffusion between the metallic electrodes and the BFO. Among the oxide electrodes, RuO_2 appears as stable conductive oxide with bulk resistivity $\leq$100 μΩ cm, large work function, high thermal and chemical stability and also acts as a good oxygen diffusion barrier [14–18]. Additional resistive inter layer like thin La_2O_3 film can be introduced for further possible reduction of the leakage currents as La_2O_3 films are reported to be mechanically stable and have high electrical breakdown field strength [19–21]. In this work, we explore the use of RuO_2 as top and bottom electrodes and La_2O_3 as resistive layer and study their systematic effects on the structure, morphology, and electrical properties of the BFO films.

2. Experimental details

RuO_2 electrodes were deposited on Pt/Ti/SiO_2/Si substrates by d.c. sputtering in an atmosphere of Ar:O_2 (1:3) at a power of 200 W for 15 min. The sputtering parameters used were described elsewhere [22]. The Ru films were annealed within the temperature range of 450–700 °C in air ambient. Thickness of the RuO_2 thin films was ~65 nm. BFO thin films were deposited on the RuO_2 coated Pt/Ti/SiO_2/Si substrates by a chemical solution deposition method. BFO solution was prepared by dissolving bismuth nitrate and iron nitrate in 2-methoxyethanol. The precursor solution was spin-coated at 4000 rpm for 20 s and dried at 240 °C. This process was repeated several times to achieve a film thickness ~550 nm. The film was annealed in a rapid thermal annealing (RTA) furnace at 550 °C in N_2 ambient. Using r.f. sputtering La_2O_3 layer of ~20 nm was developed on the BFO film and was annealed at 550 °C prior to further deposition of BFO.

The crystalline quality of the RuO_2, BFO, BFO-La_2O_3 films were assessed by XRD using the General Area Detector System (GADDS, D8-ADVANCE, Bruker), and the microstructures were studied using a field-emission scanning electron microscopy (FESEM, JSM-6700F, JEOL Ltd.). For electrical measurements, RuO_2 dot electrodes of 0.2 mm in diameter were sputter-deposited on the top surface of the BFO films through a shadow mask. The resistivity of the RuO_2 films was determined by the four-point probe measurement (MCP-T360). Dielectric measurements were carried out using an impedance analyzer (HP 4194A). Polarization–electric field (P–E) hysteresis loops were characterized by a ferroelectric tester (Radiant Inc.). Current–voltage (I–V) measurements were carried out using a Keithley 5467A electrometer. A positive bias voltage was applied to the top RuO_2 electrode. X-ray Photoelectron Spectroscopy (XPS, ESCALab 250i-XL) and the Secondary Ion Mass Spectrometry (ION-TOF SIMS IV) were used to analyze the chemical composition and the depth profiling of the stacked films. The synthesized films are defined as fol-

* Corresponding author. Tel.: +65 68748299; fax: +65 6872 0785.
E-mail address: santi-s@imre.a-star.edu.sg (S.R. Shannigrahi).

0925-8388/$ – see front matter © 2010 Elsevier B.V. All rights reserved.
doi:10.1016/j.jallcom.2010.10.135

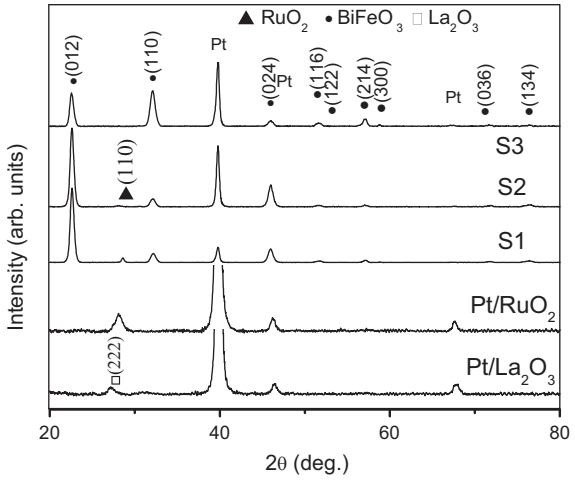

Fig. 1. XRD diffraction patterns of S1, S2, S3, RuO_2 and La_2O_3 thin films.

lows: RuO_2/BFO/La_2O_3/BFO/RuO_2/Pt/Ti/SiO_2/Si: S1, RuO_2/BFO/ RuO_2/Pt/Ti/SiO_2/Si: S2, and RuO_2/BFO/Pt/Ti/SiO_2/Si: S3.

3. Results and discussion

Fig. 1 depicts the XRD patterns of the annealed RuO_2, La_2O_3, S1, S2 and S3 films. It is observed that the RuO_2 films appear (1 1 0) preferred orientation with polycrystalline nature. The peaks are indexed according to the JCPDS card no. 40-1290. Electrical conductivity studies of the RuO_2 thin films annealed at 500–700 °C are carried out. We observe increase of conductivity for the films annealed at ≥600 °C, which attributes the increase of grain size as well as the inter layer diffusion. The conductivity of the RuO_2 films annealed at 550 °C is 9632 S cm^{-1}, which is comparable to earlier reported values [23]. For further BFO thin film depositions we use the RuO_2 films annealed at 550 °C. It is also observed that the S1, S2 and S3 films appear phase pure polycrystalline nature. The peaks are indexed according to the JCPDS card no. 82-1254. The average crystalline size of the BFO films grown with and without RuO_2 and La_2O_3 are determined using Scherrer's formula [24]. Table 1 summarizes crystalline size and dependence of preferred orientation of films. The (0 1 2)-orientation ratio is calculated using Eq. (1) [25]:

Table 1
Crystalline size and dependence of preferred orientation of films.

Sample	Preferred (0 1 2) orientation (%)	Av. crystalline size (nm)
S1 (with RuO_2 and La_2O_3)	82.06	114.42
S2 (with RuO_2, no La_2O_3)	83.63	120.00
S3 (with Pt, no La_2O_3)	44.49	91.66

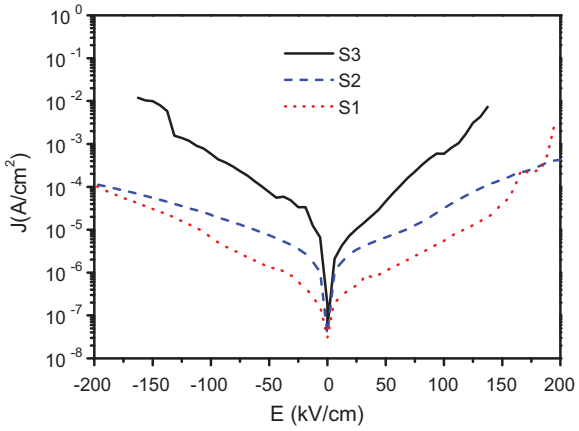

Fig. 3. Room temperature leakage properties (log$J$ vs E plots) of the S1, S2 and S3 films.

$$\text{Orientation ratio} = \frac{I(0\,1\,2)_{BFO}}{I(0\,1\,2)_{BFO} + I(1\,1\,0)_{BFO} + I(1\,1\,6)_{BFO}} \times 100 \quad (1)$$

where I(0 1 2), I(1 1 0), and I(1 1 6) refer the peak intensity of the (0 1 2), (1 1 0) and (1 1 6) orientations of the BFO films. It is observed that in the S1 and S2 films the (0 1 2) peak shows the highest intensity among the other peaks, which indicates that RuO_2 layer promotes the growth in the (0 1 2) plane. The preferred orientation in the BFO film is retained when the La_2O_3 layer is applied between the BFO films (S1). The XRD pattern of sputter-deposited La_2O_3 on Pt shows reflections belonging to cubic La_2O_3, indexed according to JCPDS card no. 22-0369. The weak peak intensities are a consequence of the thin (~40 nm) La_2O_3 layer [26]. The presence of La_2O_3 formed on BFO thin films before the stacking of another layer takes place is confirmed by XPS results, which shows that the position of the La-3$d_{5/2}$ peak is at 834.9 eV, corresponding to the exact position

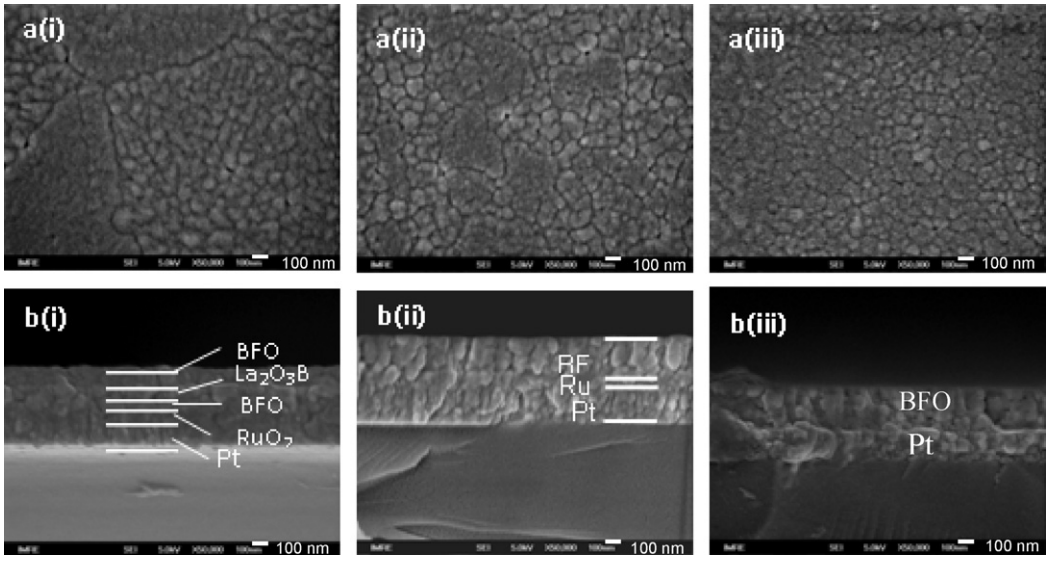

Fig. 2. SEM (a) surface morphology and (b) thickness of (i) S1, (ii) S2 and (iii) S3 films.

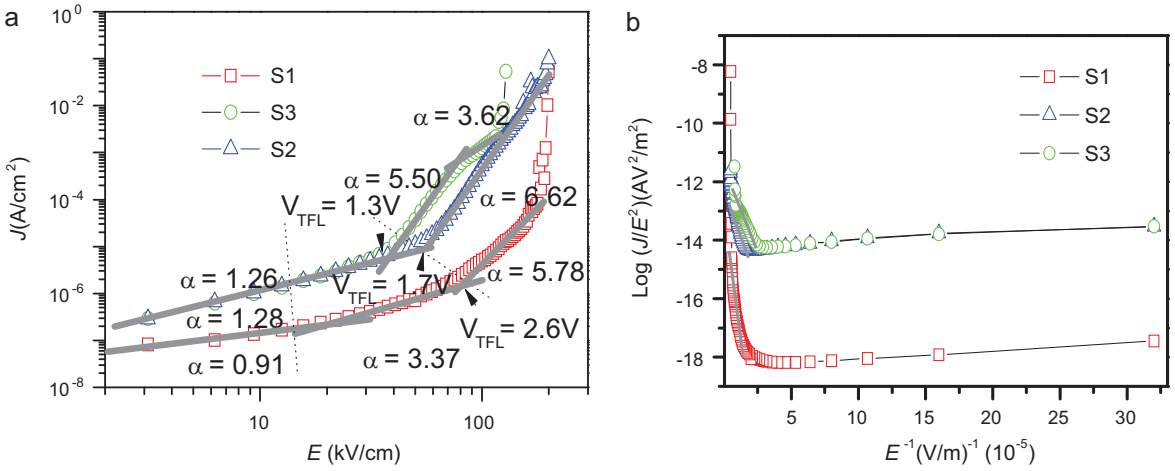

Fig. 4. (a) log(J) vs log(E) plots at the positive bias of the films measured at room temperature. The exponent, α, in $J \infty E^{\alpha}$, which is also the slope of the curve for each region in the films is shown, and (b) $\log J/E^2$ vs $1/E$ plot at the positive bias of the films measured at room temperature.

of the La-3$d_{5/2}$ peak in La_2O_3 [27,28]. We can imply that the La_2O_3 layer formed between BFO films is pure.

The surface morphologies and thicknesses of the samples are displayed in Fig. 2(a, b). It is observed that the thicknesses of all the films are very well-defined. The microstructures of S1, S2 and S3 films are equally dense. From Table 1, we observe largest grain size in S2, followed by S1 and S3 films. It again indicates that RuO_2 promotes the growth of grains. The addition of La_2O_3 may reduce the grain size slightly but generally, there is an observable difference to the grain size of the film without La_2O_3 and RuO_2 (S3). It is also observed that morphology of S1 consists of many clusters of grains growing together while grains are grown uniformly in S2 and S3 films. The difference in morphology is most likely stemmed from the La_2O_3 layer in S1. The microstructure of S1 may well resemble the rosette structure observed in Zr-rich PZT films [29–31]. Since the rosette structures are usually formed from a low nucleation rate, this may suggest that the clusters of grains found in the films are a result of different nucleation rates [30]. The La_2O_3 layer may slow down the nucleation rate of the BFO films.

Fig. 3 shows the leakage current dependence on electric field ($\log J$ vs E) plots of the S1, S2, and S3 films. The leakage current is the lowest for S1 and is the highest for S3 films. The barrier

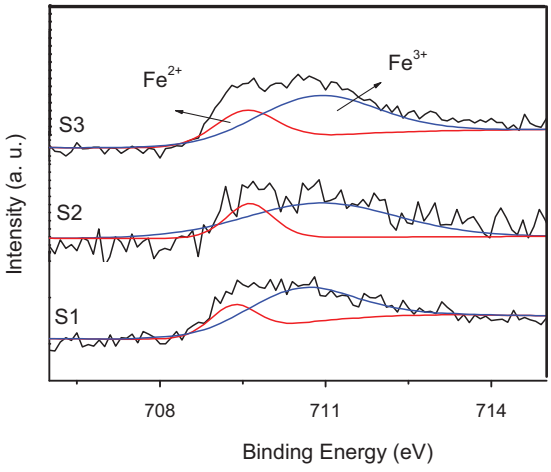

Fig. 5. XPS spectra of Fe 2p lines for S1, S2 and S3 after peak fitting.

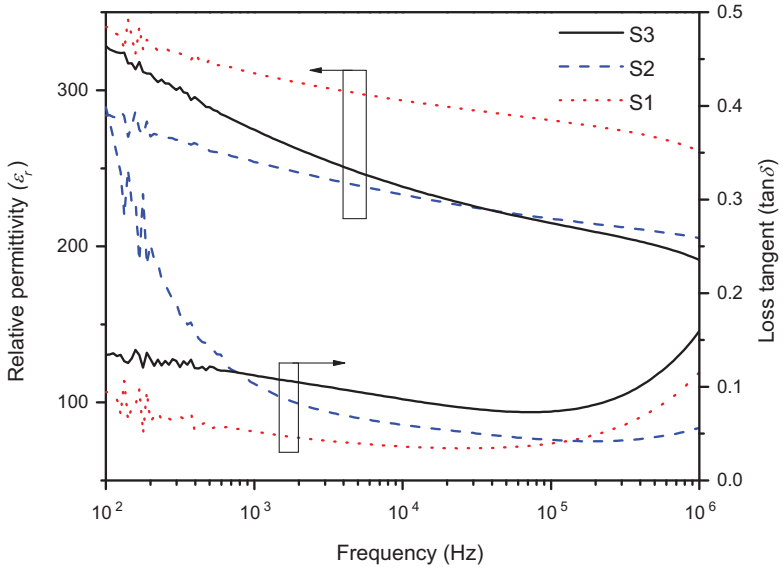

Fig. 6. Frequency dependence of relative permittivity (ε_r) and loss tangent ($\tan\delta$) for the S1, S2, and S3 films measured at room temperature.

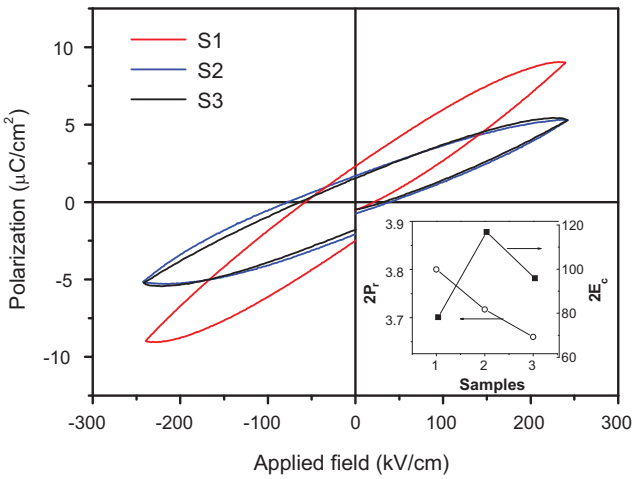

Fig. 7. *P–E* hysteresis loops of S1, S2 and S3 measured at room temperature. Insert shows the change in $2P_r$ and $2E_c$ of the same films.

layers result in lower leakage current, possibly due to the inhibition of defects such as oxygen vacancies [32]. The fluctuation in valency of Fe^{2+} and Fe^{3+} in BFO films also affects the leakage current properties in BFO thin films [8,31]. It is essential to understand the influence of La_2O_3 and RuO_2 on the electrical properties of BFO films and the origin of leakage current mechanism. The leakage current is mostly dominated by the surface-limited processes (thermionic Schottky and quantum mechanical Fowler-Nordheim currents) and the bulk-limited processes (Poole-Frenkel and Space-Charge-Limited Currents). From the log*J* vs log*E* plot in Fig. 4(a), it is observed that at low electric field (<20 kV/cm) the curve follows Ohmic behavior with the slope (α) value ~1 in each film. At higher electric field (20–100 kV/cm), the curve in each film increases with α value > 1. This type of observation in the *J–E* behaviors of the BFO films resembles the Space Charge Limited Current (SCLC) type of conduction. At low electric field, Ohmic conduction comes from the injection of electrons from the electrode or shallow traps near the conduction band of the film into the conduction band. It should be pointed out that the electrons are injected from the bottom electrode into BFO when it is positive bias. As electric field increases, the amount of injected electrons in the insulator increases, which becomes more than the thermally stimulated density of electrons, which dominate SCLC conduction. However, the slopes obtained for the films are higher than 2. The curves change according to the modified Child's law where $J \propto E^{\alpha}$, $\alpha > 1$. It is also noted that there are three different slope gradient regions for S1 and S3, and two slope gradient regions for S2 films. Each slope signifies different electron trap levels. According to Lampert [33], the voltage dependence of a film having different trap levels distributed in the band gap region is expressed in Eq. (2)

$$J = e\mu N_c \left(\frac{\varepsilon}{eN_e kT_f}\right) \frac{V^{l+1}}{d^{2l+1}} \quad (2)$$

where N_c is the effective density of states in the conduction band, μ is the charge carrier mobility, d is the film thickness, k is the Boltzmann constant and T_f is the temperature characterizing the trap distribution. For $l > 1$, or a slope of more than 2, there are deep electron trap levels in the films. The slope of ~3 for S1 in the middle range is probably due to the density of the trap levels. The slope of ~6 at higher electric field for all three samples is a result of completely filled deep traps and the double injection of charges into the bulk film. Finally, the voltage for filling up the deep electron traps is known as the trap filled limited voltage V_{TFL}, which is the transition voltage from Ohmic to modified Child's law. We found that V_{TFL} changes according to S1 > S2 > S3. This indicates that deeper traps are found in S1 compare to S2 and S3. This also implies that La_2O_3 layer between the BFO films creates deeper traps in the film. SCLC mechanism has been reported to be the main leakage mechanism in BFO films [34–38].

In addition to SCLC mechanism, Poole-Frankel (PF) conduction, which are associated with field-enhanced thermal excitation such as the release of trapped electrons or holes. Schottky emission (SE) is another leakage mechanism, which represents the field-enhanced thermionic current limited by the electrode. Therefore, it is necessary to determine whether PF or SE is a dominant leakage mechanism in the films. Both PF and SE can be expressed as Eq. (3)

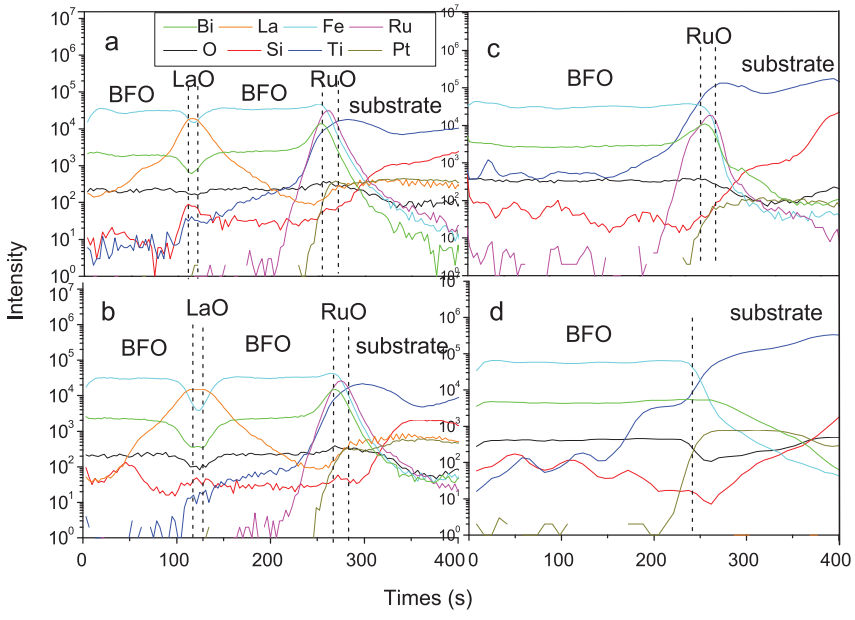

Fig. 8. SIMS depth profiles of (a) S1 before annealing, (b) S1 after annealing, (c) S2 and (d) S3 after annealing.

[39–42]:

$$\frac{J}{E} = J_o \exp\left[\frac{-(\phi_t - e\sqrt{eE/\alpha\pi\varepsilon_0\varepsilon_{opt}})}{kT}\right] \quad (3)$$

where J_o is a constant, ϕ_t is the trap ionization energy, e is the electron charge, ε_{opt} is the optical (electronic) dielectric constant of the film, ε_o is the dielectric constant of vacuum, k is the Boltzmann's constant, T is the temperature and coefficient $\alpha = 1$ for PF and 4 for SE. The conduction current is governed by PF emission or SE if the $\ln(J/E)$ vs $E^{1/2}$ plot is linear with a slope of $e\sqrt{e/(\pi\varepsilon_o\varepsilon_{opt})}/kT$ or $e\sqrt{e/(4\pi\varepsilon_o\varepsilon_{opt})}/kT$, respectively. ε_{opt} can be calculated from the slope, which can be used to calculate the optical refractive index (n) through the relation of $n = \sqrt{\varepsilon_{opt}}$. We calculate the n values for each of the slopes in the films based on the above equations. However, the n values obtained do not match with that of the BFO thin films obtained by spectroscopic ellipsometry measurement, which is about 2.5 [34,43]. This clearly indicates that PF emission or Schottky emission is not the main leakage mechanism in the films with and without the resistive layer.

Fig. 4(b) shows the log (J/E^2) vs $1/E$ plots of the films at the positive bias. We observed linear negative slopes at high electric fields (>80 kV/cm). Therefore, at higher electric fields (>80 kV/cm), Fowler-Nordheim, a surface-limit conduction is the dominant conduction mechanism in all the films. The effect of injecting charge carriers from the electrodes into an insulator layer usually occurs at high electric fields in BFO, PZT, and BST films [34,38,44].

X-ray photoelectron spectroscopy (XPS) of the S1, S2, and S3 films are shown in Fig. 5. The Fe $2p_{3/2}$ peaks are fitted into two peaks at about 709.7 and 711.2 eV, which correspond to the Fe^{2+} and Fe^{3+} states, respectively. The areas encapsulated by the curves give the concentration ratio of Fe^{2+} and Fe^{3+}. The ratios of Fe^{2+} to Fe^{3+} of S1, S2, and S3 films are 22:78, 26:74, and 59:41, respectively. The highest amount of Fe^{3+} in S1 among the three films suggests that the amount of oxygen vacancies in S1 films is the lowest, which accounts for its improved leakage current properties.

Fig. 6 plots the frequency dependence of the relative permittivity (ε_r) and loss tangent ($\tan\delta$) for the S1, S2, and S3 films, which shows highest ε_r and lowest $\tan\delta$ values as 280.8 and 0.0395 respectively at 10 kHz for the S1 films. This improvement supports the contribution of La_2O_3 and RuO_2 layers by preventing the diffusion of the substrate elements into the BFO, as in the case of a RuO_2 barrier between PZT and a metal foil [45]. The ε_r and leakage current density of the La_2O_3 thin film on $Pt/Ti/SiO_2/Si$ substrate is ~17.4 at 10 kHz and 6.06×10^{-7} A/cm^2 at 500 kV/cm, respectively. The leakage current of the current La_2O_3 film is an order higher than those obtained by atomic layer deposition and electron beam evaporation (~10^{-8} A/cm^2) [28]. This difference could be a result of the thinner La_2O_3 films formed by the latter, which range from 3.5 to 5 nm. La_2O_3 has large band gap (~5.5 eV), low leakage current, and high ε_r value make it suitable as effective sink/buffer layer for lowering of leakage current in BFO films by inhibiting the conduction of mobile charges. Therefore, the leakage current and dielectric properties of S1 and S2 films are improved.

Fig. 7 presents the P–E hysteresis loops of the samples. Comparatively better ferroelectric properties with $2P_r$ and $2E_c$ values of 3.80 μC/cm^2 and 78.22 kV/cm respectively obtained for the film S1. Inset compares the $2P_r$ and $2E_c$ values of the studied films. The possible reason for this low value is not clear at this time as both low and high values are reported in the literature [46–49]. It is also known that the measurement frequency affects the shape of the hysteresis and the polarization values too. The poorer electrical properties in S3 film is due to the obvious Si and Ti diffusion from the substrates into the BFO layers in all the samples are analyzed using SIMS as shown in Fig. 8. There is no diffusion of Ru and La into BFO layers in S1, S2, and S3 films observed after annealing. This confirms absence of intermediate phase formation between RuO_2 and BFO films [50,51].

4. Conclusions

We employ RuO_2 and La_2O_3 as oxide electrodes and resistive layers to synthesize BFO films on $Pt/Ti/SiO_2/Si$ substrates using a chemical solution deposition method. The BFO films with RuO_2 and La_2O_3 layers show preferred (0 1 2)-orientation growth with dense morphology. RuO_2 and La_2O_3 resistive layers improve the value of ε_r and P_r and reduce leakage currents of the BFO films. It is found that diffusions of Ti and Si from the substrate into the BFO films are impeded by the RuO_2 barrier layer. XPS analysis also shows that the BFO films grown with the barrier layers contain smaller amount of Fe^{2+} than those without the barrier layers, which cause lower oxygen vacancies in the former and result improved leakage current properties. Space-charge-limited current dominates in all the films at electric field below ≤80 kV/cm and surface-limit conduction current dominates at higher electric field >80 kV/cm.

References

[1] R. Ramesh, N. Spaldin, Nat. Mater. 6 (2007) 21.
[2] J. Wu, J. Wang, J. Alloys Compd. 507 (2010) L4.
[3] G. Catalan, J.F. Scott, Adv. Mater. 21 (2009) 2463.
[4] T. Xian, H. Yang, X. Shen, J.L. Jiang, Z.Q. Wei, W.J. Feng, J. Alloys Compd. 480 (2009) 889.
[5] H.W. Jang, S.H. Baek, D. Ortiz, C.M. Folkman, C.B. Eom, Y.H. Chu, P. Shafer, R. Ramesh, V. Vaithyanathan, D.G. Schlom, Appl. Phys. Lett. 92 (2008) 062910.
[6] X.J. Lou, X.J.M. Zhang, M.S.A.T. Redfern, J.F. Scott, Phys. Rev. Lett. 97 (2007) 177601.
[7] S.R. Shannigrahi, A. Huang, N. Chandrasekhar, D. Tripathy, A.O. Adeyeye, Appl. Phys. Lett. 90 (2007) 022901.
[8] A. Huang, S.R. Shannigrahi, V.K.X. Lin, Eletrochem. Solid-State Lett. 11 (2008) G47.
[9] X. Zhang, Y. Sui, X. Wang, Y. Wang, Z. Wang, J. Alloys Compd. 507 (2010) 157.
[10] S.K. Singh, H. Ishiwara, K. Sata, K. Maruyama, J. Appl. Phys. 102 (2007) 094109.
[11] N.M. Murari, R. Thomas, A. Winterman, R.E. Melgarejo, S.P. Pavunny, R.S. Katiyar, J. Appl. Phys. 105 (2009) 084110.
[12] A.Z. Simões, R.F. Pianno, E.C. Aguiar, E. Longo, J.A. Varela, J. Alloys Compd. 479 (2009) 274.
[13] D. Lebeugle, D. Colson, A. Forget, M. Viret, Appl. Phys. Lett. 91 (2007) 022907.
[14] C.C. Lee, J.M. Wu, C.P. Hsiung, Appl. Phys. Lett. 90 (2007) 182909.
[15] A.Z. Simoes, A.H.M. Gonzalez, E.C. Aguiar, C.S. Riccardi, E. Longo, J.A. Varela, Appl. Phys. Lett. 93 (2008) 142902.
[16] J. Liu, M. Li, L. Pei, J. Wang, B. Yu, X. Wang, X. Zhao, J. Alloys Compd. 493 (2010) 544.
[17] H. Liu, X. Wang, J. Alloys Compd. 485 (2009) 769.
[18] L.W. Martin, Y.-H. Chu, R. Ramesh, Mater. Sci. Eng. R 68 (2010) 89.
[19] Y. Du, Z.X. Cheng, M. Shahbazi, E.W. Collings, S.X. Dou, X.L. Wang, J. Alloys Compd. 490 (2010) 637.
[20] H. Zhang, X. Chen, T. Wang, F. Wang, W. Shi, J. Alloys Compd. 500 (2010) 46.
[21] Y. Kim, K. Miyauchi, S.-I. Ohmi, K. Tsutsui, H. Iwai, Microelectronics Journal 36 (2005) 41.
[22] J.S. Ye, H.F. Cui, X. Liu, T.M. Lim, W.D. Zhang, F.S. Shen, Small 1 (2005) 560.
[23] W.T. Lim, K.R. Cho, C.H. Lee, Thin Solid Films 348 (1999) 56.
[24] B.D. Culity, Element of X-ray Diffraction, Addison-Wesley, Reading, MA, 1978.
[25] M.P. Klug, L.E. Alexander, X-ray Diffraction Procedure for Polycrystalline and Amorphous Materials, Wiley, New York, 1974, p. 634.
[26] M. Nieminen, M. Putkonen, L. Niinisto, Appl. Surf. Sci. 174 (2001) 155.
[27] S.J. Jo, J.S. Ha, N.K. Park, D.K. Kang, B.H. Kim, Thin Solid Films 513 (2006) 253.
[28] J.B. Cheng, A.D. Lia, Q.Y. Shaoa, H.Q. Ling, D. Wu, Y. Wang, Y.J. Bao, M. Wang, Z.G. Liu, N.B. Ming, Appl. Surf. Sci. 233 (2004) 91.
[29] Z.J. Wang, Y. Aoki, L.J. Yan, H. Kokawa, R. Maeda, J. Cryst. Growth 267 (2004) 92.
[30] M. Sreemany, A. Bose, S. Sen, Mater. Chem. Phys. 115 (2009) 453.
[31] S.Y. Chen, I.W. Chen, J. Am. Ceram. Soc. 81 (1998) 97.
[32] N.M. Murari, A. Kumar, R. Thomas, R.S. Katiyar, Appl. Phys. Lett. 92 (2008) 132904.
[33] M. Lampert, Phys. Rev. 103 (1956) 1648.
[34] H. Yang, M. Jain, N.A. Suvorova, H. Zhou, H.M. Luo, D.M. Feldmann, P.C. Dowden, R.F. Depaula, S.R. Foltyn, Q.X. Jia, Appl. Phys. Lett. 91 (2007) 072911.
[35] T. Kawae, Y. Terauchi, H. Tsuda, M. Kumeda, A. Morimoto, Appl. Phys. Lett. 94 (2009) 112904.
[36] N.M. Murari, R. Thomas, R.E. Melgarejo, S.P. Pavunny, R.S. Katiyar, J. Appl. Phys. 106 (2009) 014103.
[37] C.F. Chung, J.P. Lin, J.M. Wu, Appl. Phys. Lett. 88 (2006) 242909.
[38] Z. Zhong, H. Ishiwara, Appl. Phys. Lett. 95 (2009) 112902.
[39] K.H. Ahn, S.S. Kim, S.G. Baik, J. Appl. Phys. 92 (2002) 421.

[40] Y.P. Wang, T.Y. Tseng, J. Appl. Phys. 81 (1997) 6762.
[41] J.G. Simmons, Phys. Rev. 155 (1967) 657.
[42] M. Sedlar, M. Sayer, D.T. Amm, J. Appl. Phys. 80 (1996) 367.
[43] F. Chen, B. Li, R.A. Dufresne, R. Jammy, J. Appl. Phys. 90 (2001) 1898.
[44] Y. Masuda, T. Nozaka, Jpn. J. Appl. Phys. 43 (2004) 6576.
[45] D.J. Kim, D. Shen, S.H. Yoon, S.Y. Choe, D.Y. Kaufman, Ceram. Int. 34 (2008) 1261.
[46] G.W. Pabst, L.W. Martin, Y.H. Chu, R. Ramesh, Appl. Phys. Lett. 90 (2007) 072902.
[47] S.K. Singh, K. Maruyama, H. Ishiwara, J. Phys. D: Appl. Phys. 40 (2007) 2705.
[48] M.M. Kumar, V.R. Palkar, K. Srinivas, S.V. Suryanarayana, Appl. Phys. Lett. 76 (2000) 2764.
[49] X. Qi, J. Dho, R. Tomov, M.G. Blamire, J.L.M. Driscoll, Appl. Phys. Lett. 86 (2005) 062903.
[50] J. Gao, L. Zheng, J. Zeng, C. Lin, Jpn. J. Appl. Phys. 37 (1998) 5126.
[51] K.T. Jacob, G. Rajitha, V.S. Saji, Bull. Mater. Sci. 32 (2009) 313.